Available online at www.sciencedirect.com
SCIENCE DIRECT®
Journal of Nuclear Materials 340 (2005) 247–258
journal of nuclear materials
www.elsevier.com/locate/jnucmat

Hardening and microstructural evolution in A533B steels under high-dose electron irradiation

K. Fujii [a,*], K. Fukuya [a], N. Nakata [a], K. Hono [b], Y. Nagai [c], M. Hasegawa [c]

[a] *Institute of Nuclear Safety System, 64 Sata, Mihama-cho, Mikata-gun, Fukui 919-1205, Japan*
[b] *National Institute for Materials Science, Tsukuba, Ibaraki 305-0045, Japan*
[c] *Tohoku University, Oarai-cho, Higashi Ibaraki-gun, Ibaraki 311-1313, Japan*

Received 20 May 2004; accepted 22 December 2004

Abstract

Commercial A533B steels (0.12, 0.16 wt% Cu) irradiated at 290 °C up to 22 mdpa with 5 MeV electrons were examined by hardness measurements, positron lifetime spectroscopy, the coincidence Doppler broadening (CDB) technique and three-dimensional atom probe microanalysis (3DAP). The radiation-induced hardening increased with electron dose and lay on the same trend of neutron-induced hardening within data scatter. CDB measurements revealed that clustering of Cu atoms occurred at doses over 1 mdpa and proceeded with increasing dose. 3DAP results showed that well-defined Cu-rich precipitates with a diameter of less than 2 nm were formed at doses of 10 and 22 mdpa. The precipitates had a shell structure consisting of a Cu–Fe core region and a surrounding Mn–Ni–Si shell, which are similar to those formed under neutron irradiation. The size and number density of the precipitates were consistent with previous neutron data. Positron lifetime spectroscopy showed that no microvoids were formed. The electron irradiation caused almost the same hardening efficiency and evolution of Cu-rich precipitates as those under neutron irradiation on a dpa basis.

PACS: 61.80.Fe; 61.82.Bg; 61.72.−y; 81.40.Cd; 78.70.B; 61.16.Fk

1. Introduction

Radiation embrittlement of reactor vessel steels is one of the essential degradation issues in the continued long-life safe operation of light water reactors (LWRs). To forecast the long-life integrity of vessel steels considering various material variables and irradiation conditions, it is necessary to use predictive models based on physical mechanisms [1–3]. This needs a sound understanding of the physical mechanisms of microstructural evolution and influence of irradiation conditions such as neutron flux and spectra. To study the effects of flux and spectra, irradiation experiments using charged particles such as ions and electrons are useful as well as material test reactors [4–9].

Electron irradiation is known to provide unique information on the effects of primary knock-on atom (PKA) energy spectra on microstructural evolution and hardening. Electron displacements produce low-energy

* Corresponding author. Tel.: +81 770 37 9114; fax: +81 770 37 2009.
E-mail address: fujiik@inss.co.jp (K. Fujii).

0022-3115/$ - see front matter © 2005 Elsevier B.V. All rights reserved.
doi:10.1016/j.jnucmat.2004.12.008

PKAs with a resultant high concentration of freely migrating defects (fmds), which is different from cascade displacements under fast neutron irradiation. Irradiation experiments with electrons have been applied to radiation effect studies on low alloy steels from two viewpoints: PKA energy effects on microstructural evolution and assessment of gamma-ray irradiation effects on hardening and embrittlement of reactor vessel steels. Electron displacements are actually induced in reactor vessel steels, where high-energy gamma rays generate energetic electrons through the processes of Compton scattering and electron-positron pair production. The contribution of gamma ray (electron) irradiation to radiation hardening in ferritic alloys has been examined over the last decade [10–13]. Since the dpa cross-sections for gamma rays are much smaller than those of neutrons [14–16], the relative contribution of gamma ray is typically small in reactors. However the contribution is dependent on reactor core characteristics and the water gap distance between core and components and becomes greater than 50% in some particular cases [12,13]. Such was the case for the vessel of the high flux isotope reactor (HFIR). A greater contribution of gamma ray-induced displacement due to the high-level gamma ray field in HFIR was considered to be the cause of the unexpected embrittlement of the vessel. This hypothesis was confirmed by experimental results demonstrating that hardening occurs in Fe–Cu alloys and commercial ferritic steels under electron irradiation up to several mdpa [6–9].

An interesting implication of these electron irradiation experiments is that the hardening efficiency of electron irradiation is equal to the hardening efficiency of fast neutron irradiation on a dpa basis. The fraction of point defects per unit dpa that survive immediate annihilation is much greater for low-energy-PKA electron irradiation. The surviving defects under cascade damage is ~30% of the NRT dpa in pressure vessels of light water reactors [17]. If the formation of Cu-rich precipitates dominates hardening and if the amount of fmds determines the clustering process, electron irradiation should result in a greater hardening per dpa than fast neutron irradiation in Cu-containing ferritic alloys. This issue of PKA energy effects is related to the role of cascade damage in microstructural evolution. The observed equal hardening efficiency in electron and neutron irradiation suggests that cascade damage might enhance microstructural evolution such as solute clustering. However, there have been few studies on characterizations of microstructures under electron irradiation. Auger et al. reported the formation of pure Cu precipitates (~100% Cu) in Fe–1.4Cu alloys after electron irradiation to 0.054 mdpa at 290 °C, but the formation of fine defused Cu-rich precipitates (45–95% Cu) after neutron irradiation to 75 mdpa [18,19]. They also found no Cu clusters in a Fe–0.1Cu alloy electron-irradiated to 1.2 mdpa, but found dilute Cu-rich precipitates (35% Cu) after neutron irradiation to 75 mdpa. Mathon et al. reported the difference in growth behavior of Cu clouds in a Fe–1Cu model alloy between electron and neutron irradiation [20]. These observations for model Fe–Cu alloys indicated that cascade damage has undefined effects of solute clustering although the dpa level was much lower for electron irradiation.

For elucidation of PKA energy effects on hardening in ferritic steels, a clearer understanding of fine-scale microstructural evolution in ferritic steels is needed. The dpa reached in the previous studies was less than several mdpa, where microstructural features such as Cu-rich precipitates might not be well developed in commercial steels. This paper describes the results of high-dose electron irradiations up to 22 mdpa at 290 °C in commercial vessel steels. Microstructures were characterized using three-dimensional atom probe (3DAP) microanalysis, and positron annihilation spectroscopy (PA) including both positron lifetime measurement and the coincidence Doppler broadening technique (CDB). The results are compared with those of the same steels irradiated in a commercial reactor and in a material test reactor to 50–100 mdpa [21].

2. Experimental procedures

2.1. Materials and irradiation

Two heats of A533B steel, named steel A and steel B, were used in this study. The chemical compositions are shown in Table 1. The heat treatment conditions are described elsewhere [21]. Plate specimens measuring $48 \times 10 \times 1$ mm were machined from the blocks of steels A and B. The specimens were mechanically polished using wet grinding on SiC papers down to 1000 grit and then electro-plated with chromium in order to protect the surface oxidation from the ozone atmosphere produced by electron irradiation in air.

Table 1
Chemical composition of steels (wt%)

	C	Si	Mn	P	S	Cr	Ni	Mo	Cu	Fe
A	0.12	0.25	1.20	0.014	0.015	0.58	0.08	0.54	0.12	Balance
B	0.17	0.29	1.45	0.011	0.017	0.55	0.11	0.50	0.16	Balance

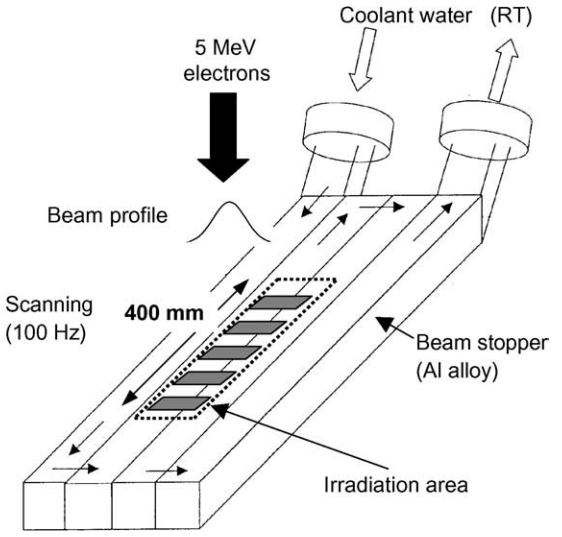

Fig. 1. Schematic figure of electron irradiation system.

Irradiations were carried out with 5 MeV electrons using an accelerator at NFI Irradiation Service, Ltd., Japan. Fig. 1 shows the schematic figure of the irradiation system. About ten specimens were mounted on a water-cooling beam stopper (aluminum alloy) with silver paste and screws in order to keep contact during irradiation. The irradiation area was 400 mm in the beam scanning direction and 50 mm in the specimen length. The scanning rate was 100 cycles per second. The electron beam had a Gaussian intensity profile along the specimen length. The relative beam intensity to the peak was 90% at 5 mm away from the peak position. In this irradiation system, the temperature of each specimen was determined by beam heating in the specimen and the stopper, and heat transfer to the stopper. Specimen-to-specimen deviation of temperature occurred due to the difference in contact between each specimen and stopper. Thus the temperature of each specimen was monitored during irradiation with a thermocouple spot-welded to the center position of each specimen. The specimens whose temperature variation was within ±10 °C from the average temperature during whole irradiation time, were selected and used for further examinations. The average temperature of the selected specimens ranged from 230 to 300 °C.

Incident electron flux was 4 to 7×10^{18} e/m^2/s at the peak of the beam intensity profile. This corresponds to a dpa rate of $1.7–2.9 \times 10^{-8}$ dpa/s, assuming an averaged dpa cross-section through the specimen thickness of 43 barns (NRT model with a displacement energy of 40 eV). The difference in dpa rate between the incident and back surfaces of a specimen was estimated to be 20%, considering the decrease of electron energy in the material due to energy loss. Total dpa level was set at 0.1, 1, 3, 10 and 22 mdpa. The maximum dose was achieved with 360 h of irradiation.

2.2. Examinations

Hardness measurements were conducted for all the specimens, and PA measurements and 3DAP analyses for specimens irradiated at around 290 °C (LWR-relevant temperature). For measurements and analyses, the specimen area of 10×10 mm at the center of the specimen length was used, where the variation of the incident beam intensity was less than 10%. Preliminary measurements of hardness distribution along both the length and thickness of a specimen revealed that no notable variation of hardness had occurred in the 10×10 mm area.

Vickers hardness was measured with a 500 g load on the center of the specimen thickness. The hardness value of each specimen was determined by averaging over ten measurements.

PA measurements using the CDB technique [22,23] and positron lifetime spectroscopy were performed on plates of $7 \times 5 \times 0.5$ mm cut from irradiated specimens. The surface layers were removed by chemical polishing in 5% hydrofluoric acid in hydrogen peroxide at 10 °C. The positron source was ^{22}Na. The samples attached to the positron source were positioned between two Ge detectors located at an angle of 180° relative to each other. Total counts greater than 4×10^6 were accumulated for 12 h in each measurement. In accordance with the standard CDB technique, the ratio curve of the measured spectra to that for a well-annealed pure Fe as the reference were calculated against P_L, where P_L is the longitudinal component of the positron–electron momentum along the direction of the gamma ray emission. The S- and W-parameters are defined as the ratios of low-momentum ($|P_L| < 4 \times 10^{-3} m_0 c$) and high-momentum ($18 \times 10^{-3} m_0 c < |P_L| < 30 \times 10^{-3} m_0 c$) regions to the total region, respectively. The S-parameter increases and the W-parameter decreases when positrons are trapped at vacancy-type defects. When positrons annihilate with Cu-3d electrons, the W-parameter increases. The other important parameter from CDB measurements is the fraction of the positron annihilation with Cu electrons (I_{Cu}). This is estimated as follows. In the high-momentum region, the CDB spectrum $N_{Fe–Cu}(P_L)$ is approximately expressed as

$$N_{Fe–Cu}(P_L) \approx (1-x)N_{Fe}(P_L) + xN_{Cu}(P_L),$$

where $N_{Fe}(P_L)$ and $N_{Cu}(P_L)$ is the CDB spectrum of pure Fe and pure Cu, respectively. The parameter x can be interpreted as the average fraction of Cu atoms at the site where positron annihilation takes place. Thus the ration curve becomes

$$R_{Fe–Cu}(P_L) \approx (1-x) + xR_{Cu}(P_L),$$

where $R_{Cu}(P_L) = N_{Cu}(P_L)/N_{Fe}(P_L)$ is the ration curve of pure Cu. The x obtained by fitting this equation to the measured CDB ratio curve is the fraction of positron annihilation with Cu electrons, referred as I_{Cu} in this paper.

Positron lifetime measurements were carried out using a conventional fast-fast spectrometer with a time resolution of 190 ps (full width at half maximum). Total counts were about 3×10^6 for each measurement. After subtracting the source component and background, the spectra were decomposed into two components (shorter component: τ_1 and longer component: τ_2).

3DAP measurements were carried out using energy compensated position-sensitive atom probe facilities at the National Institute for Material Science, Japan [24]. The instrument consists of a reflectron energy compensator, a position sensitive detector and a high-resolution flight time detector. The error originating from the evaporation aberration is less than 0.2 nm. The mass resolution ($m/\Delta m$) was over 200 full widths at half maximum. Samples measuring $0.4 \times 0.4 \times 10$ mm cut from irradiated specimens were electro-polished to form needles in a solution of 5% perchloric acid, glycerin and ethanol. Final electro-polishing was performed using 2% perchloric acid in 2-butoxyethanol. Measurements were conducted at a sample temperature of 60 K with the pulse fraction of 0.15 for (1 1 0) orientations to the detector.

3. Results

3.1. Hardness measurements

Hardness (Hv) and radiation-induced hardening (ΔHv) is shown in Table 2. The standard deviation of Hv was 6–17 for over ten measurements. Fig. 2 shows dose dependence of ΔHv in steels A and B. The radiation hardening increased with increasing dose and reached ~50 at 22 mdpa in both steels. No significant difference with irradiation temperature was observed within data scatter. This weak temperature dependence was consistent with the data shown by Tobita et al. in electron-irradiated Fe–0.6%Cu alloy at 250–320 °C [9].

3.2. CDB measurements

Fig. 3 shows the CDB ratio curves for unirradiated and irradiated samples, together with the curve for well-annealed pure Cu as a reference. The broad peaks around $24 \times 10^{-3} m_0 c$ are characteristic of Cu-3d electrons, indicating clustering of Cu atoms. The peak was observed in steel A after irradiation at 1, 10 and 22 mdpa, and became clearer for higher doses. No peak was observed for unirradiated and 0.1 mdpa irradiated samples. The ratios near $P_L = 0$ increased with increasing dose up to 10 mdpa. This increase in the low-momentum region means the increase in the number of vacancy-type defects in the materials. However, the ratio at $P_L = 0$ showed a decrease at 22 mdpa. Steel B showed similar changes to steel A whereas the CDB ratio curve at 10 mdpa was close to that at 22 mdpa.

These changes with electron dose are shown in Fig. 4, which plots the dose dependence of S- and W-parameters, along with the fraction of the positron annihilation with Cu electrons (I_{Cu}) estimated from the height of the peak in the high-momentum region of the CDB ratio curves. The S-parameters increased with increasing dose up to 10 mdpa because of the increase in positron trapping at vacancy-type defects. The W-parameters decreased with increasing dose up to 1 mdpa and in

Table 2
Results of hardness measurements

Material	ID	Temperature (°C)	Dose rate ($\times 10^{-8}$ dpa/s)	Dose (mdpa)	Hv	ΔHv
A	A0	–	–	0	196	–
	A16	230	2.3	1	209	13
	A8	245	2.0	10	233	37
	A3	250	2.7	1	205	9
	A5	255	2.0	3	219	23
	A13	290	2.9	0.1	197	1
	A15	290	2.3	1	215	19
	A9	290	2.0	10	233	37
	A11	290	1.7	22	245	49
B	B0	–	–	0	201	–
	B22	235	2.7	1	217	16
	B23	265	2.7	1	209	8
	B24	270	2.0	3	224	23
	B27	270	2.0	10	244	43
	B36	285	2.3	1	207	6
	B33	290	2.9	0.1	203	2
	B32	300	1.7	22	253	51

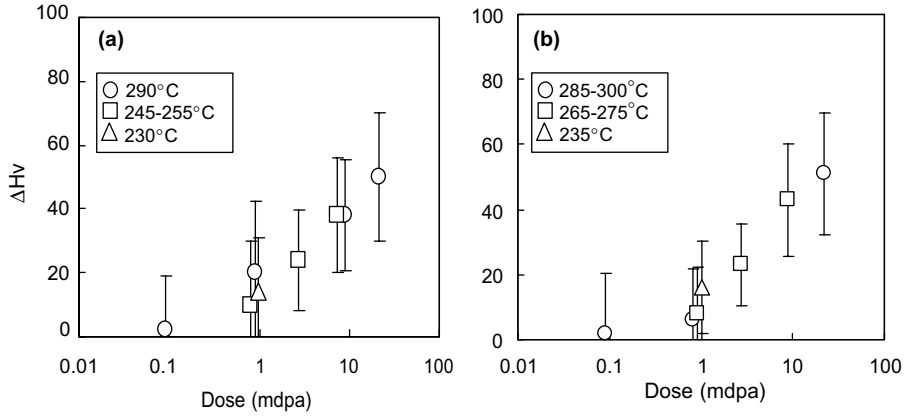

Fig. 2. Dose dependence of radiation-induced hardening (ΔHv) in (a) steel A and (b) steel B under electron irradiation. The dashed line shows a power law expression $\Delta Hv \sim (dpa)^{1/3}$.

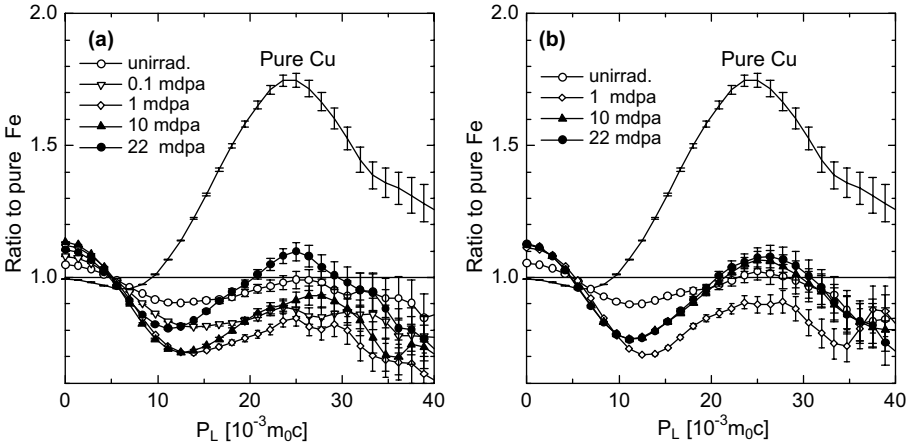

Fig. 3. CDB ratio curves for (a) steel A and (b) steel B after electron irradiation at 290 °C.

turn increased with increasing dose. The decrease in *W*-parameter means that the positrons are mainly trapped and annihilated at vacancy-type defects. On the other hand, the increase in *W*-parameter means that the positron annihilation with Cu electrons becomes predominant. The apparent saturation and decrease of the *S*-parameters at higher dose are due to the positron annihilation with Cu electrons. The I_{Cu} started to increase at 0.1–1 mdpa and increased with increasing dose, reaching to ~60% at 22 mdpa in steel A. The changes in *S*- and *W*-parameters in steel B were very similar to those in steel A. The *W*-parameter and I_{Cu} were slightly higher for steel B, probably because Cu clustering was pronounced due to a higher Cu content in steel B.

The CDB measurements indicated that accumulation of vacancy-type defects and Cu aggregation occurs in steels A and B irradiated at 290 °C.

3.3. Positron lifetime measurements

Fig. 5 shows the dose dependence of average positron lifetime (τ_{av}), shorter component (τ_1), longer component (τ_2), and relative intensity of τ_2 component (I_2). Since the positron lifetime spectra for steel A irradiated to 1 and 10 mdpa and for steel B irradiated to 1, 10 and 22 mdpa could not divided into two components, the single life time was plotted as τ_2 and τ_{av} for them in Fig. 5. The unirradiated value of τ_{av} was 145 and 155 ps for steels A and B, respectively. These values were greater than 110 ps for pure Fe matrix, indicating that there were open-volume defects even in unirradiated steels. τ_2 and I_2 increased with increasing dose to 1 mdpa followed by saturation. The saturating value of τ_2 is ~170 ps, which is smaller than the lifetime of single vacancies in Fe (180 ps). Vacancy-type clusters such as microvoids

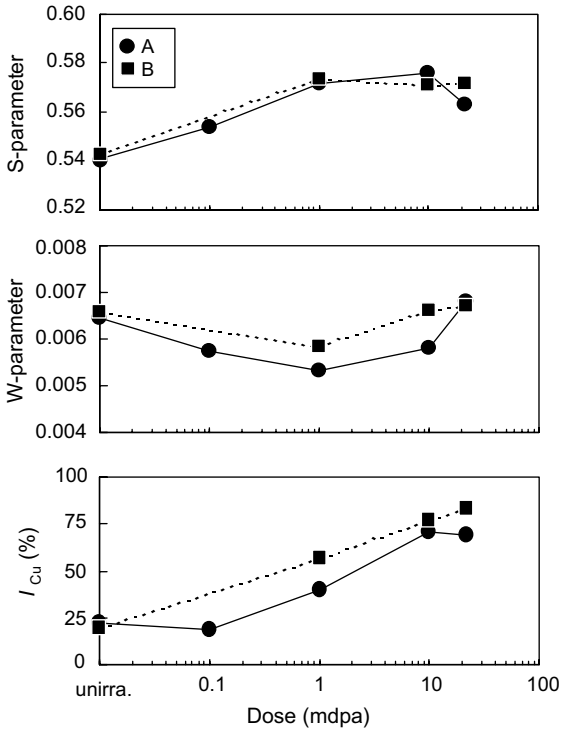

Fig. 4. Dose dependence of *S*-, *W*-parameter and I_{Cu} after electron irradiation at 290 °C.

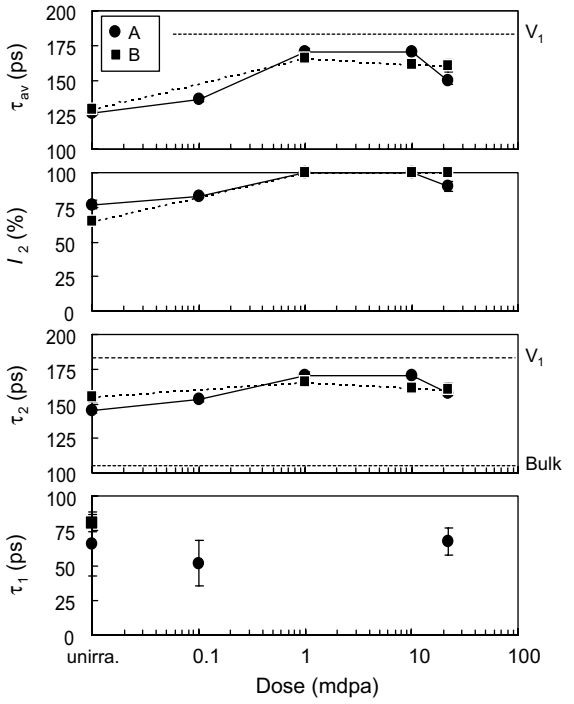

Fig. 5. Dose dependence of average positron lifetime (τ_{av}), shorter component (τ_1) and longer componentτ_2) and relative intensity of τ_2 component (I_2) after electron irradiation at 290 °C.

were not formed under the present electron irradiation. At doses higher than 10 mdpa, the lifetime tended to decrease. This reflects an increase in positron annihilation at Cu clusters, where the positron lifetime is estimated to be comparable to that in pure Fe [23].

3.4. 3DAP analyses

Fig. 6 shows a set of elemental maps from steel A irradiated to 22 mdpa. Fig. 7 shows an enlarged view of the largest one among the four Cu-rich regions indicated in Fig. 6. Aggregation of Cu atoms was clearly detected and accompanied by enrichment of Mn, Ni and Si atoms. In the present analyses Cu-rich precipitates are defined as clusters containing more than five Cu atoms with Cu–Cu distances of less than 0.7 nm. Under this definition, a number of Cu-rich precipitates were observed in both steels A and B irradiated to 22 mdpa. The largest precipitates contained 22 Cu atoms in both steels. The number density in steels A and B, estimated by the number of detected precipitates divided by the specimen volume, was approximately 5 and 16×10^{23} m^{-3}, respectively. In steel A irradiated to 10 mdpa, a limited number of precipitates were detected whereas the precipitate was accompanied with enrichment of Mn, Ni and Si. No Cu-rich precipitates were detected in steel A irradiated to 1 mdpa. In order to check Cu clustering at lower doses, the randomness of Cu and Mn atom distribution was checked in steel A irradiated to 1 and 10 mdpa using the χ^2 statistic analysis for composition frequency distribution in a block size of 90 atoms [25]. The level of significance for Cu and Mn was 90% and 95%, respectively, at 1 mdpa, and 5% and 1%, respectively, at 10 mdpa. The results mean that the distribution of Cu and Mn atoms was almost random at 1 mdpa but not random at 10 mdpa. Thus the clustering of Cu atoms was not evidenced at 1 mdpa but evidenced at 10 mdpa.

The size and composition of Cu-rich precipitates were determined using the radius of gyration defined by the following equation:

$$\text{Radius of gyration} = \sqrt{\frac{1}{n}\sum_{i=1}^{n}\left\{(x_i - x_c)^2 + (y_i - y_c)^2 + (z_i - z_c)^2\right\}},$$

where x_c, y_c and z_c are the co-ordinates of the center of mass, n is the total number of Cu atoms contained in each Cu-rich precipitate, and x_i, y_i and z_i are the positions of the Cu atoms. Fig. 8 shows the radial composition distribution of the largest Cu-rich precipitate containing 22 Cu atoms observed in steel A irradiated

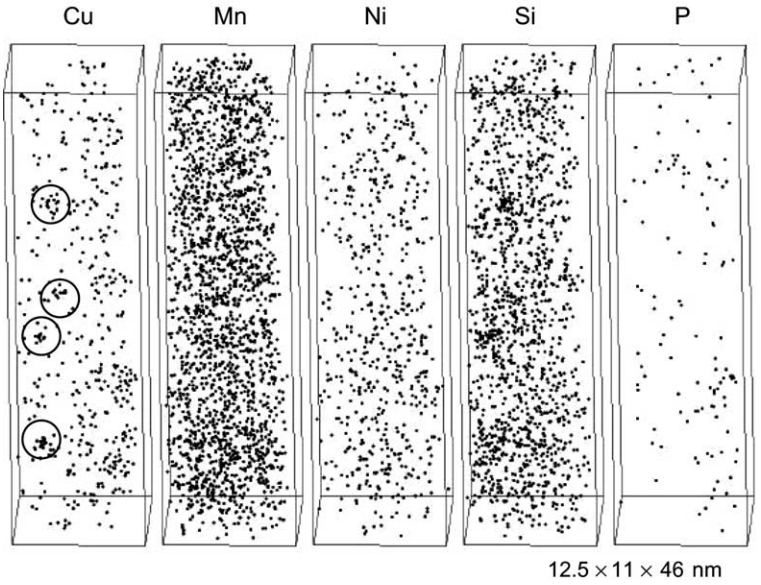

Fig. 6. 3D atom map of solutes in $12.5 \times 11 \times 46$ nm region in steel A after electron irradiation to 22 mdpa at 290 °C. The arrows indicate Cu-rich precipitates.

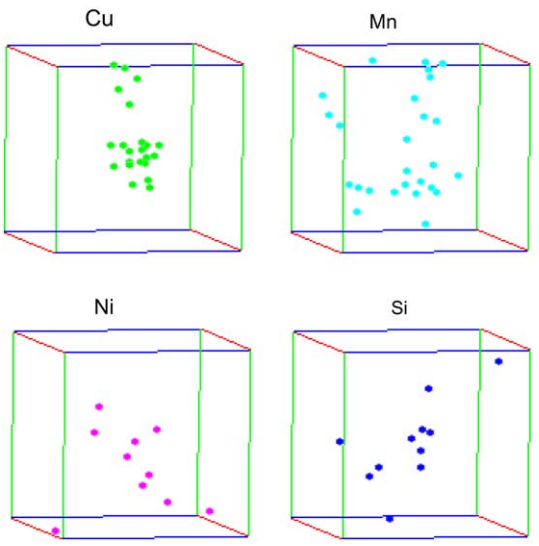

Fig. 7. Enlarged 3D atom map ($3 \times 3 \times 3$ nm) showing a Cu-rich precipitate in Fig. 6.

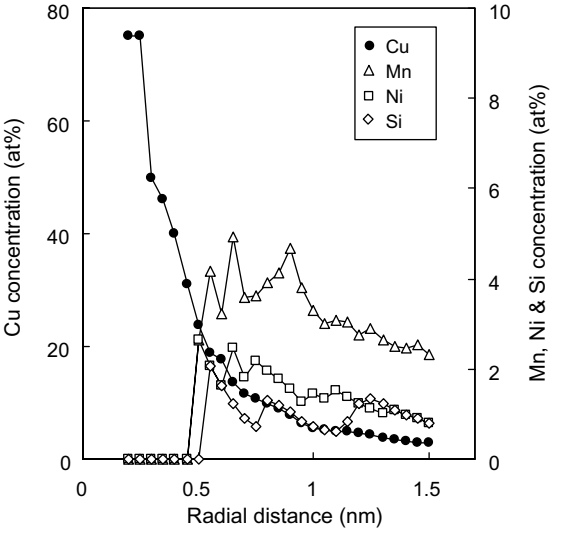

Fig. 8. Radial distribution of solutes in the Cu-rich precipitate shown in Fig. 7.

to 22 mdpa. A double-layered structure, called a shell structure, was clearly observed. In the core region (<0.4 nm), Fe and Cu atoms were detected whereas no other elements existed. The Cu concentration was as high as 70% in the core region. Outside the core region, Mn, Ni and Si were enriched. This shell structure was commonly detected, being independent of the precipitate size in both steels A and B. The composition of Cu-rich precipitates, defined as the atomic concentration within a sphere of the radius of Cu gyration, was Fe–(3–12)Cu–(1–4)Mn–(0–2)Ni–(0–12)Si in steels A and Fe–(4–14)Cu–(2–10)Mn–(0–9)Ni–(0–3)Si in steel B. No precipitates contained P atoms in the present irradiated steels.

Fig. 9 shows the distribution of the radius of gyration at 22 mdpa. The range of the radius was 0.5–0.8 nm for steel A and 0.3–0.8 nm for steel B. The ranges of the size

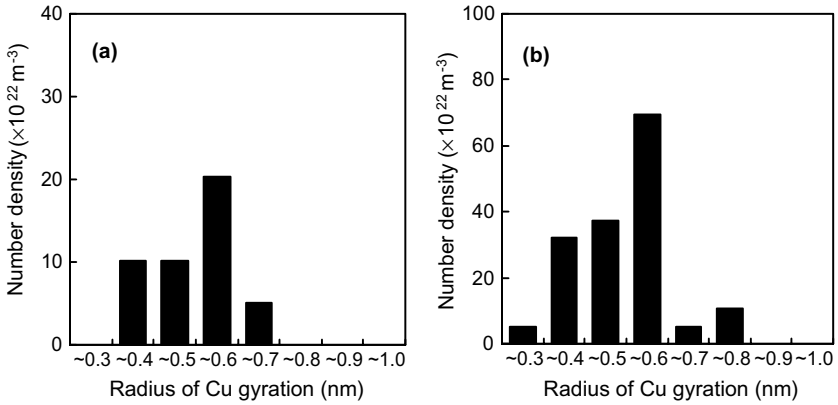

Fig. 9. Size distribution of Cu-rich precipitates in (a) steel A and (b) steel B irradiated to 22 mdpa at 290 °C.

distribution and the mean sizes were almost the same for steels A and B. However, the number density in steel B ($\sim 16 \times 10^{23}$ m^{-3}) was higher than that in steel A ($\sim 5 \times 10^{23}$ m^{-3}), suggesting that the formation of Cu clusters was more pronounced due to a higher Cu content in steel B.

4. Discussion

4.1. Evolution of fine-scale microstructures under electron irradiation

The combination of PA measurements and 3DAP analyses yielded detailed information on fine-scale microstructural evolution in the steels under electron irradiation at 290 °C. At the early stage of irradiation, vacancies started to accumulate in the matrix as monovacancies, probably trapped at solute atoms, up to 1 mdpa. This was confirmed from the monotonous increase in S-parameter and average positron lifetime (τ_{av}). At the same time, Cu atoms aggregated along with vacancy accumulation. The earliest indication was detected in the increase in I_{Cu} from 0.1–1 mdpa from the unirradiated level. The Cu clusters had already formed at 1 mdpa, which was confirmed from the fact that the W-parameter started to increase at 1 mdpa. The hardness increase was detected at 1 mdpa. With further irradiation, the formation of Cu-rich precipitates continued with increasing dose. This was directly confirmed by 3DAP analyses and was also consistent with the increase in hardness, W-parameter and I_{Cu} at 10–22 mdpa. The Cu-rich precipitates with a diameter of 1–2 nm have a shell structure consisting of a Fe–Cu core and a Mn–Ni–Si shell. At this stage the S-parameter and lifetime in turn decrease with increasing dose, since most of the positrons annihilate with Cu-3d electrons at Cu-rich precipitates resulting in a relative decrease in short-life and low-momentum components in PA spectra. At the highest dose in this study (22 mdpa), Cu-rich precipitates were well defined with a number density in the order of 10^{24} m^{-3} whereas no microvoids were formed.

Most of the data from the different techniques are consistent with each other. However the dose where Cu aggregation was detected was different between the CDB measurements and 3DAP analyses. The results of the CDB measurements in steel A suggested that Cu aggregation occurred at <1 mdpa judging from the increase in I_{Cu}, and was more clearly confirmed at 1 mdpa judging from the increase in W-parameter. On the other hand, no Cu clusters were detected at 1 mdpa in the 3DAP analyses. Cu atoms randomly distribute with the significance level of 95% at this dose. Nagai et al. showed that the positron is confined at aggregations of five Cu atoms and that complete confinement is achieved when the pure Cu precipitate grows to ~0.5 nm in diameter containing 59 Cu atoms [23]. The observed low I_{Cu} value (~30%) at 1 mdpa implies that the diameter and/or density of Cu-rich precipitates were small and below the detection limit of the 3DAP analyses due to the collective efficiency of evaporated ions and spatial resolution.

At 22 mdpa, the I_{Cu} value was ~70% in the CDB measurements. This means that ~30% of the positrons annihilate with electrons of elements other than Cu. The size and number density of Cu-rich precipitates, ~1.2 nm and 10^{23-24} m^{-3}, are likely to be sufficient to trap almost all positrons at the precipitates if the precipitates consist of pure Cu. The 3DAP analyses showed that the atomic fraction of Cu was as high as ~70 at.% in the core region of the precipitates whereas the precipitates contained a high average amount of Fe atoms, nearly 90% within the radius of the Cu gyration. If we assume that all positrons are trapped at the core of precipitates, the observed I_{Cu} value is likely to be consistent with the composition of the Cu-rich precip-

itates determined by 3DAP analyses. However, it is uncertain whether such apparent consistency is commonly obtained in other irradiated alloys or steels. There are other possibilities: a significant number of free mono-vacancies exist in matrix and trap positrons, otherwise the trapping efficiency for positrons of diffuse multi-element precipitates would be less than that of pure Cu precipitates. Further experiments are needed to clarify these issues, which are related to the nature and barrier strength of fine-scale precipitates.

4.2. Comparison between electron and neutron irradiation

Hardening and precipitation behavior of the present commercial steels were examined after neutron irradiation at 290 °C to high-doses (50 and 100 mdpa) in a pressurized water reactor (PWR) and a material test reactor (MTR) [21]. Although the dose rate and final dose in the neutron irradiation were not the same as those in the present irradiation, comparison was made to get insight on cascade effects.

Fig. 10 shows a plot of radiation-induced hardening (ΔHv) at 290 °C in steels A and B under the present electron irradiation together with the previous neutron irradiation [21]. The trend line shown in the figure is based on a power law expression, $\Delta Hv \sim (dpa)^{1/3}$. The neutron data lie on the trend line of the electron data within the data scatter band, whereas similar hardening level (ΔHv ~50) was achieved at 22 mdpa under the electron irradiation and at 50 mdpa under the neutron irradiation. Regarding microstructures, the present experiments confirmed that well-defined Cu-rich precipitates, which have a shell structure, Fe–Cu core and Mn–Ni–Si-rich shell, were formed under electron irradiation at 290 °C in medium Cu commercial steels. The structure and composition of the precipitates were basically the same as those observed in commercial steels irradiated with neutrons [21,25,28–31]. The result that no micorvoid formation occurs under electron irradiation at 290 °C is also consistent with the reported results for commercial steels after neutron irradiation at near 300 °C [32–34]. Table 3 summarizes data for Cu-rich precipitates in steels A and B at 290 °C under the present electron irradiation, together with the previous neutron irradiation in which the microstructure was examined using small angle neutron scattering (SANS) measurements and 3DAP analyses. For comparison, the composition in Table 3 was defined as the atomic concentration within a 1.5 nm cube containing the center of precipitates. The electron irradiation produced precipitates with a smaller diameter and a higher density than the neutron irradiation. This is not simply because the electron dose was smaller than the neutron dose. The precipitates density in steel B electron-irradiated to 22 mdpa was actually higher than that MTR-irradiated to 94 mdpa. With respect to the composition of Cu-rich precipitates, high concentration of Fe was commonly detected in both electron and neutron irradiation. The concentration of Cu and Ni was lower for the electron irradiation.

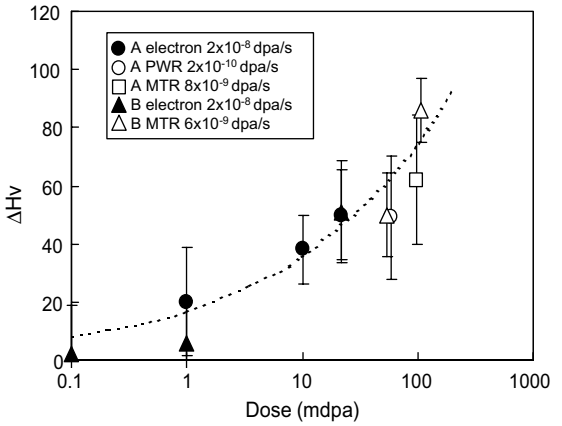

Fig. 10. Plot of radiation-induced hardening in steels A and B under electron irradiation at 290 °C together with the previous neutron irradiation data [21].

It is well known that radiation hardening in low alloy steels containing Cu is attributed to Cu-rich precipitates and, so called, matrix damage. In the present electron irradiation, although it was confirmed that no

Table 3
Data of Cu-rich precipitates formed in steels A and B irradiated with electrons and neutrons at 290 °C

Material	Irradiation	Dose rate (dpa/s)	Dose (mdpa)	Diameter (nm)	Density ($\times 10^{23}$ m^{-3})	Average composition (at.%)	Volume fraction
A	5 MeV e$^-$	2×10^{-8}	1	ND	ND	–	–
			10	~1	~0.5	93Fe–3Cu–2Mn–1Ni–1Si	<0.001
			22	1–2	5	90Fe–4Cu–3Mn–1Ni–2Si	~0.002
	PWR	2×10^{-10}	58	2.6	4	63Fe–15Cu–8Mn–7Ni–4Si	0.0038
	MTR	8×10^{-9}	99	2.1	10	80Fe–11Cu–4Mn–4Ni–1Si	0.0046
B	5 MeV e$^-$	2×10^{-8}	22	1–2	16	90Fe–5Cu–4Mn–1Ni–1Si	~0.004
	MTR	4×10^{-9}	54	2.1	11	74Fe–11Cu–4Mn–7Ni–2Si	0.0053
		8×10^{-9}	94	2.1	13	78Fe–9Cu–5Mn–6Ni–3Si	0.0064

microvoid existed, the existence of other components such as interstitial clusters and their relative contribution to hardening were not clarified. Thus before discussing similarities of hardening and Cu precipitation between electron and neutron irradiation, the relative contribution of Cu-rich precipitates to hardening is discussed. In the neutron-irradiated steel A, it was demonstrated from post-irradiation annealing experiments that the Cu-rich precipitate was the main contributor to hardening in the neutron-irradiated steels [21]. Almost 70% of hardening could be attributed to the Cu-rich precipitates in the present steels irradiated to 50–100 mdpa. Since the size and density of Cu-rich precipitates and hardening level in the electron-irradiated steels were comparable to those in the neutron-irradiated steels, Cu-rich precipitates are expected to be dominant in hardening of the electron-irradiated steels. To check this point, the relation of hardening (ΔHv) and volume fraction (VF) of Cu-rich precipitates is plotted in Fig. 11, together with literature data from commercial steels containing higher Cu (0.15–0.5%) irradiated with neutrons [28,35–38]. Since the literature data were obtained from high Cu steels at relatively low doses (less than 30 m dpa), it is reasonable to assume that the Cu-rich precipitate is the dominant source. Both the electron and neutron data in steels A and B lay on a general trend line ($\Delta Hv \sim VF^{1/2}$) by the dashed line, indicating that the hardening in these steels depended on the amount of Cu-rich precipitates as the literature data did. This implies that the Cu-rich precipitates are the dominant hardening source in the present steels under both electron and neutron irradiation.

It is known that the hardening due to Cu-rich precipitates depends on their size, number density and chemical composition, which depend on irradiation conditions such as dose rate and PKA spectrum. The dose rate of the electron irradiation was 3 to 4 times higher than that of the MTR irradiation and two orders higher than that of the PWR irradiation. The dose rate effects on Cu-rich precipitates under neutron irradiation have been reported [1,25–28], in that neutron irradiation at a higher dose rate produces Cu-rich precipitate with smaller diameter and higher density. From the data for neutron-irradiated steel A in Table 3, higher-dose-rate MTR irradiation gave a smaller diameter than PWR irradiation even though the dose was higher for MTR irradiation. The concentrations of Cu, Ni, Mn and Si in the precipitates for PWR irradiation were higher than those for MTR irradiation. Table 3 revealed that the electron irradiation produced Cu-rich precipitates with smaller size, higher density and more dilute solutes concentration than the neutron irradiation. These trends are well consistent with the dose rate effects under neutron irradiation. The differences in size, density and composition for the Cu-rich precipitate between the electron and neutron irradiation are likely to attribute to dose rate effects, since the basic morphology of the precipitates was quite similar.

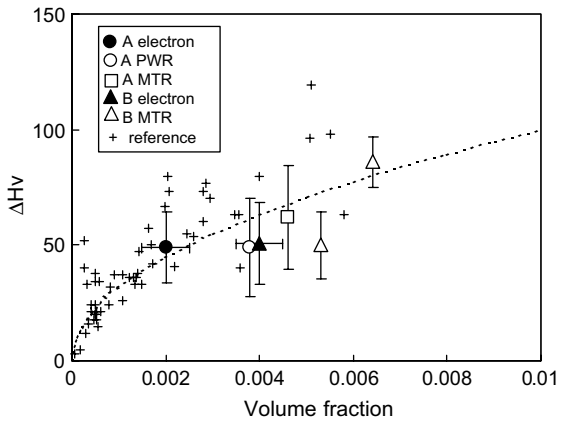

Fig. 11. Relation of hardening (ΔHv) and volume fraction (VF) of Cu rich precipitates together with literature data from commercial steels irradiated with neutrons [28,35–38]. The dashed line shows a power law expression $\Delta Hv \sim (VF)^{1/2}$.

Considering variation in the size and density of the Cu-rich precipitates due to dose rate effects, the hardening trend against dose should differ with irradiation and material combinations. However, a general trend curve seems to exist in Fig. 10 within scatter of hardness measurement. One of the reasons for this is that the differences in precipitates size and density induced by different irradiation conditions are not so large in commercial steels at the present dose range. For example, as shown in Table 3, two orders difference of dose rate (PWR at 10^{-10} dpa/s vs. MTR at 10^{-8} dpa/s) resulted in small difference in size (2.6 vs. 2.1 nm) in steel A. Furthermore, since dose rate effects change the size and density in opposite direction, such trade-off effects in a narrow range may result in a small difference in hardening trend compared to the measurement scattering. These considerations are consistent with the fact that the hardening in Cu-containing steels at a dose rate ranging from 10^{-10} to 10^{-8} dpa/s under neutron irradiation is relatively insensitive to dose rate effects compared to that at higher and lower dose rate ranges [2,26], as well as the fact that the hardening due to Cu precipitation generally depends on the volume fraction ($VF^{1/2}$) as shown in Fig. 11.

As a whole, Fig. 10 suggests that the hardening efficiency of electron irradiation is almost the same as that of neutron irradiation on the dpa basis. Similar hardening efficiencies between neutron irradiation and electron irradiation have been reported in model Fe–Cu alloys and low alloy steels at doses of less than 5 mdpa [6–9]. The present results provide more clear evidence in medium Cu commercial steels at higher doses.

The present experiments revealed that electron irradiation produces essentially the same solute clustering and hardening effects as neutron irradiation in medium Cu commercial steels. The equal hardening efficiency in electron and neutron irradiation originated from the almost equal degree of evolution of Cu-rich precipitates when the Cu-rich precipitates are the dominant hardening source. The microstructures evolve through common processes at least in agglomeration of solutes and vacancies for both electron and neutron irradiation. Isolated vacancies, which can easily migrate at 290 °C, bind Cu atoms and the complexes agglomerate to form Cu clusters. Although the origin of the shell structure is still unclear, the present results suggest, at least, that cascade mixing under high-energy PKAs is not necessary to form such structure. The earlier comparisons of Cu clustering between electron and neutron irradiation might be improved by using high-dose experiments, since the dose of electron irradiation in the literature, typically less than 3 mdpa, was too low to cause nucleation and development of well-defined Cu precipitates in alloys containing ~0.1% Cu. The formation of Cu-rich precipitates is controlled by diffusion of Cu atoms via the vacancy mechanism. Hence the evolution of Cu-rich precipitates is determined by the cumulative vacancy mobility, which is proportional to the number of fmds. The number of fmds under electron irradiation is expected to be higher than that under fast neutron irradiation as is widely accepted. The present results suggest that the cascade displacement under high-PKA-energy irradiation would enhance Cu aggregation through processes such as locally enhanced net vacancy mobility near cascades.

Finally, a recent study by Kudo et al. revealed that interstitial type dislocation loops ($b = a\langle 1\,0\,0\rangle$) were formed in Fe–0.15%Cu alloy under electron irradiation to 22 mdpa at 290 °C [39]. This suggested that such loops might be formed, acting as hardening source in electron-irradiated commercial steels. Although quantitative data of interstitial components as matrix damage are quite scarce due to technical difficulty to identify them [40], such experimental efforts are needed to fully understand the cascade effects on hardening and embrittlement in commercial steels.

5. Conclusion

High-dose electron irradiation up to 22 mdpa was conducted on medium Cu commercial vessel steels at 290 °C to examine radiation-induced hardening and fine-scale microstructural evolution. The results were compared with the previous reactor irradiation data of the same steels. Almost equal hardening efficiency was revealed in electron and neutron irradiation on a dpa basis, supporting earlier conclusions at lower doses. The formation of well-defined Cu-rich precipitates, which dominated hardening, was evidenced from positron annihilation and atom probe measurements. The density, size, composition and structure of the precipitates were consistent with those observed under neutron irradiation considering dose rate effects. Overall, the results support the view that electron irradiation has essentially the same effects of hardening and solute clustering as neutron irradiation on a dpa basis.

Acknowledgements

The authors would like to thank E. Ikuta, NFI Irradiation Service, Ltd., for performing electron irradiation and also to thank S. Yanakita, NIMS, for assistance in atom probe analyses.

References

[1] S. Ishino, in: S. Ishino et al. (Eds.), Proceedings of International Symposium on Mechanisms of Material Degradation and Non-Destructive Evaluation in Light Water Reactors, Institute of Nuclear Safety System, 2002, p. 29.
[2] G.R. Odette, G.E. Lucas, Radiat. Eff. Def. Solids 144 (1998) 189.
[3] W.J. Phythian, C.A. English, J. Nucl. Mater. 205 (1993) 162.
[4] H. Shibamoto, T. Kitao, H. Matsui, M. Hasegawa, S. Yamaguchi, A. Kimura, in: S.T. Rosinski et al. (Eds.), Effects of Radiation on Materials: 20th International Symposium, ASTM STP 1405, ASTM, 2001, p. 722.
[5] Q. Yu, G.S. Was, D. Alexander, R. Odette, in: Proceedings of 10th International Conference on Environmental Degradation of Materials in Nuclear Power Systems – Water Reactors, NACE, 2002.
[6] I. Remec, J.A. Wang, F.B.K. Kann, K. Farrell, J. Nucl. Mater. 217 (1994) 258.
[7] D.E. Alexander, L.E. Rehn, K. Farrell, R.E. Stoller, J. Nucl. Mater. 228 (1996) 68.
[8] K. Farrell, R.E. Stoller, P. Jung, H. Ullmaier, J. Nucl. Mater. 279 (2000) 77.
[9] T. Tobita, M. Suzuki, A. Iwase, K. Aizawa, J. Nucl. Mater. 299 (2001) 267.
[10] L.K. Mansur, K. Farrell, J. Nucl. Mater. 170 (1990) 236.
[11] D.E. Alexander, L.E. Rehn, J. Nucl. Mater. 209 (1994) 212.
[12] D.E. Alexander, L.E. Rehn, J. Nucl. Mater. 217 (1994) 213.
[13] F.A. Garner, L.R. Greenwood, P. Roy, in: R.K. Nanstad et al. (Eds.), Effects of Radiation on Materials: 18th International Symposium, ASTM STP 1325, ASTM, 1999, p. 52.
[14] K. Fukuya, I. Kimura, J. Nucl. Sci. Technol. 40 (2003) 423.
[15] N.P. Baumann, in: Proceedings 7th ASTM-EURATOM Symposium on Reactor Dosimetry, 1992, p. 689.
[16] J. Kwon, A.T. Motta, Ann. Nucl. Energy 27 (2000) 1627.
[17] R.E. Stoller, Nucl. Eng. Des. 195 (2000) 129.

[18] P. Auger, P. Pareige, S. Welzel, J.-C. Van Deysen, J. Nucl. Mater. 280 (2000) 331.
[19] P. Auger, P. Pareige, M. Akamatsu, J.-C. Van Deysen, J. Nucl. Mater. 211 (1994) 194.
[20] M.H. Mahon, A. Barbu, F. Dunstetter, F. Maury, N. Lorenzelli, C.H. de Novion, J. Nucl. Mater. 245 (1997) 224.
[21] K. Fukuya, K. Ohno, H. Nakata, S. Dumbill, J.M. Hyde, J. Nucl. Mater. 312 (2003) 163.
[22] Y. Nagai, M. Hasegawa, Z. Tang, A. Hempel, K. Yubuta, T. Shimamura, Y. Kawazoe, A. Kawai, F. Kano, Phys. Rev. B 61 (2000) 6574.
[23] Y. Nagai, Z. Tang, M. Hasegawa, T. Kanai, M. Saneyasu, Phys. Rev. B 63 (2001) 134110.
[24] K. Hono, Acta Mater. 47 (1999) 3127.
[25] J.M. Hyde, D. Ellis, C.A. English, T.J. Williams, in: S.T. Rosinski et al. (Eds.), Effects of Radiation on Materials: 20th International Symposium, ASTM STP 1405, ASTM, 2001, p. 262.
[26] G.R. Odette, G.E. Lucas, D. Kligensmith, in: R.K. Nanstad et al. (Eds.), Effects of Radiation on Materials: 18th International Symposium, ASTM STP 1325, ASTM, 1999, p. 88.
[27] T.J. Williams, D. Ellis, in: S.T. Rosinski et al. (Eds.), Effects of Radiation on Materials: 20th International Symposium, ASTM STP 1405, ASTM, 2001, p. 8.
[28] R.G. Carter, N. Soneda, K. Dohi, J.M. Hyde, C.A. English, W.L. Server, J. Nucl. Mater. 298 (2001) 211.
[29] P. Auger, P. Pareige, M. Akamatsu, D. Blavette, J. Nucl. Mater. 225 (1995) 225.
[30] P. Auger, P. Pareige, S. Welzel, J.-C. Van Duysen, J. Nucl. Mater. 280 (2000) 331.
[31] M.K. Miller, K.F. Russell, M.A. Sokolov, R.K. Nanstad, J. Nucl. Mater. 320 (2003) 177.
[32] G. Braer, L. Liszkay, B. Molnar, R. Krause, Nucl. Eng. Des. 127 (1991) 47.
[33] C. Gil Lopes, A.P. de Lima, N. Ayres de Campos, J.V. Fernandes, G. Kogel, P. Sperr, W. Trifshauser, D. Pachur, J. Nucl. Mater. 161 (1989) 1.
[34] K. Ghazi-Wakili, U. Zimmermann, J. Brunner, P. Tipping, W.B. Waeber, F. Heinrich, Phys. Status Solidi (a) 102 (1987) 153.
[35] J.T. Buswell, W.J. Phythian, R.J. McElroy, S. Dumbill, P.H.N. Ray, J. Mace, R.N. Siclair, J. Nucl. Mater. 225 (1995) 196.
[36] G. Solt, F. Friedrich, W.B. Waldemar, P. Tipping, in: A.S. Kumar et al. (Eds.), Effects of Radiation on Materials: 16th International Symposium, ASTM STP 1175, ASTM, 1993, p. 444.
[37] J.T. Buswell, E.A. Little, R.N. Sinclair, in: R.K. Nanstad et al. (Eds.), Effects of Radiation on Materials: 18th International Symposium, ASTM STP 1325, ASTM, 1999, p. 30.
[38] T.J. Williams, W.J. Phythian, in: D.S. Gelles et al. (Eds.), Effects of Radiation on Materials: 17th International Symposium, ASTM STP 1270, 1996, p. 191.
[39] T. Kudo, R. Kasada, A. Kimura, K. Hono, K. Fukuya, H. Matsui, Mater. Trans. 45 (2004) 338.
[40] K. Fujii, K. Fukuya, J. Nucl. Mater. 336 (2005) 323.